Ice Cloud Retrievals and Analysis with the Compact Scanning Submillimeter Imaging Radiometer and the Cloud Radar System during CRYSTAL FACE

K. FRANKLIN EVANS

Program in Atmospheric and Oceanic Sciences, University of Colorado, Boulder, Colorado

JAMES R. WANG, PAUL E. RACETTE, AND GERALD HEYMSFIELD

NASA Goddard Space Flight Center, Greenbelt, Maryland

LIHUA LI

University of Maryland, Baltimore County, Baltimore, Maryland

ABSTRACT

Submillimeter-wave radiometry is a new technique for determining ice water path (IWP) and particle size in upper-tropospheric ice clouds. The first brightness temperatures images of ice clouds above 340 GHz were measured by the Compact Scanning Submillimeter Imaging Radiometer (CoSSIR) during the Cirrus Regional Study of Tropical Anvils and Cirrus Layers (CRYSTAL) Florida Area Cirrus Experiment (FACE) campaign in July 2002. CoSSIR operated with 12 channels from receivers at 183, 220, 380, 487, and 640 GHz. CoSSIR and the nadir-viewing 94-GHz Cloud Radar System (CRS) flew on the NASA ER-2 airplane based out of Key West, Florida. A qualitative comparison of the CoSSIR brightness temperatures demonstrates that the submillimeter-wave frequencies are more sensitive to anvil ice cloud particles than are the lower frequencies. A Bayesian algorithm, with a priori microphysical information from in situ cloud probes, is used to retrieve the IWP and median mass equivalent sphere particle diameter (D_{me}). Microwave scattering properties of random aggregates of plates and aggregates of frozen droplets are computed with the discrete dipole approximation (DDA) and an effective medium approximation tuned to DDA results. As a test of the retrievals, the vertically integrated 94-GHz radar backscattering is also retrieved from the CoSSIR data and compared with that measured by the CRS. The integrated backscattering typically agrees within 1–2 dB for IWP from 1000 to 10 000 g m^{-2}, and while the disagreement increases for smaller IWP, it is typically within the Bayesian error bars. Retrievals made with only the three 183- and one 220-GHz channel are generally as good or better than those including 380 ± 6.2 and 640 GHz, because the CoSSIR submillimeter-wave channels were much noisier than expected. An algorithm to retrieve profiles of ice water content and D_{me} from CRS and CoSSIR data was developed. This Bayesian algorithm also retrieves the coefficients of an IWC–radar reflectivity power-law relation and could be used to evaluate radar-only ice cloud retrieval algorithms.

1. Introduction

There are no methods for the accurate global remote sensing of ice cloud mass for climate studies (Wielicki et al. 1995). Global measurements of vertically integrated cloud ice mass [ice water path (IWP)] are important for evaluating climate model parameterizations and studying the upper-tropospheric water budget. Visible and infrared satellite remote sensing techniques for ice clouds (e.g., Rossow and Schiffer 1999; Stubenrauch et al. 1999) have poor accuracy for high IWP clouds, which contain much of the total cloud ice mass. Thermal infrared methods saturate with moderate optical depths and can only determine particle size (and, hence, IWP) for an effective radius below about 50 μm. Solar reflection methods cannot distinguish ice from underlying water cloud optical depth, cannot measure thinner clouds over bright surfaces, and can only retrieve particle sizes near the cloud top for optically thicker clouds, resulting in biased IWP retrievals. Millimeter-wave radar backscattering from CloudSat (Stephens et al. 2002), when combined with visible reflectance measurements, will improve the IWP retrieval accuracy; however, the radar's nadir view provides coverage that is too sparse to obtain a global climatology of the cloud ice mass with regional-scale resolution.

Corresponding author address: Dr. K. Franklin Evans, University of Colorado, 311 UCB, Boulder, CO 80309-0311.
E-mail: evans@nit.colorado.edu

TABLE 1. CoSSIR channel characteristics.

Channel (GHz)	Center frequency (GHz)	Bandwidth (GHz)	System temperature (K)	NEΔT* (calculated) (K)	NEΔT** (measured) (K)
183.3 ± 1.0	1.0	0.5	2500	0.55	0.90
183.3 ± 3.0	3.0	1.0	1390	0.23	0.61
183.3 ± 6.6	6.6	1.5	1050	0.15	0.75
220	2.5	3.0	1760	0.16	0.84
380.2 ± 0.8	0.75	0.7	3460	0.63	NA
380.2 ± 1.8	1.80	1.0	8440	1.23	4.01
380.2 ± 3.3	3.35	1.7	4820	0.55	4.25
380.2 ± 6.2	6.20	3.6	6670	0.52	4.99
487.25 ± 0.8	0.68	0.35	4650	1.17	2.57
487.25 ± 1.2	1.19	0.48	3890	0.85	1.66
487.25 ± 3.3	3.04	2.93	4600	0.40	2.05
640	2.5	3.0	16 000	1.33	4.90

* Calculated values based on the receiver system temperature measured in the laboratory and 50-ms integration time.
** Measured from the calibration target data on the 1 Jul flight with the same integration time.

Theoretical studies (Gasiewski 1992; Evans and Stephens 1995b; Evans et al. 1998) have suggested that millimeter-wave and submillimeter-wave radiometry have the potential for accurate retrievals of cloud IWP and characteristic ice particle size. The technology of submillimeter-wave radiometry has lagged the theory, and only recently have the first submillimeter measurements of ice clouds been made from aircraft. The Far Infrared Sensor for Cirrus (FIRSC), which is a Fourier transform spectrometer with a cryogenic bolometer detector (Vanek et al. 2001), made measurements from 300 to above 1000 GHz during several campaigns. The sensitivity of FIRSC's bolometric detector precludes cross-track scanning, and the brightness temperature noise is high below about 800 GHz. The submillimeter-wave cloud –ice radiometer, developed at the Jet Propulsion Laboratory (Evans et al. 2002), has heterodyne receivers at 183, 325, 448, and 643 GHz, but has not yet been flown. The millimeter-wave imaging radiometer (MIR; Racette et al. 1996) had receivers at 89, 150, 183, and 220 GHz. Several groups have developed cloud IWP retrieval algorithms for MIR data at 89, 150, and 220 GHz (Liu and Curry 2000; Deeter and Evans 2000; Weng and Grody 2000). A 340-GHz channel was later added to MIR, and significant brightness temperature depressions were observed from Arctic cirrus (Wang et al. 2001).

The Compact Scanning Submillimeter Imaging Radiometer (CoSSIR) is a new instrument with 15 channels from 183 to 640 GHz. CoSSIR flew for the first time on the National Aeronautics and Space Administration (NASA) ER-2 aircraft during the Cirrus Regional Study of Tropical Anvils and Cirrus Layers (CRYSTAL) Florida Area Cirrus Experiment (FACE) deployment out of Key West, Florida, in July 2002. One of the objectives of CRYSTAL FACE was the improvement and validation of remote sensing methods for near-tropical convective anvil ice clouds. The 94-GHz nadir-viewing Cloud Radar System (CRS) flew with CoSSIR on the ER-2. In this paper we describe

CoSSIR and show examples of millimeter-wave and submillimeter-wave brightness temperature depressions that are associated with convective anvils in the south Florida region. We describe the retrieval of the ice water path and median volume equivalent sphere diameter (D_{me}), using a Bayesian algorithm with updated prior information on ice cloud microphysics. The appendixes describe the in situ ice particle size distribution analysis and the particle shape modeling that are used in the prior distribution for the retrieval. Retrievals from CoSSIR of integrated radar reflectivity are compared with CRS data to evaluate the CoSSIR retrievals. Last, a new algorithm is presented to retrieve profiles of ice water content (IWC) and D_{me} from the combination of CoSSIR and CRS data.

2. Data

During the month of July 2002, a major field campaign—CRYSTAL FACE—was conducted by NASA over the region surrounding Florida. Six aircraft, equipped with a variety of remote sensing instruments and in situ probes, participated in this campaign; all of these aircraft were stationed in Key West. The NASA ER-2 aircraft was one of the six and was equipped with a suite of highly sophisticated remote sensors, including the CoSSIR and the 94-GHz CRS (Li et al. 2004) that measures radar reflectivity profiles of cloud particles.

The CoSSIR is a new, total-power radiometer that has a total of six receivers and 15 channels. Twelve channels are horizontally polarized at the frequencies of 183.3 ± 1.0, 183.3 ± 3.0, 183.3 ± 6.6, 220 ± 2.5, 380.2 ± 0.8, 380.2 ± 1.8, 380.2 ± 3.3, 380.2 ± 6.2, 487.25 ± 0.8, 487.25 ± 1.2, 487.25 ± 3.3, and 640 ± 2.5 GHz, and 3 channels are vertically polarized at 487.25 ± 0.8, 487.25 ± 1.2, and 487.25 ± 3.3 GHz (see Table 1). All six heterodyne receivers use highly integrated subharmonically pumped Schottky barrier mixers. The local oscillators use thermally stabilized Gunn diode oscilla-

tors followed by varactor-diode multiplier chains (except for the 183 receiver, which just uses a Gunn diode oscillator). Images are generated by rotating the receiver scanhead assembly on dual-axes gimbals, which can be programmed to perform across-track scans as well as conical scans at a fixed incidence angle. During CRYSTAL FACE the receiver was programmed in an across-track scan mode so that coincident measurements with the CRS and Moderate Resolution Imaging Spectroradiometer (MODIS) airborne simulator could be made. The 3-dB beamwidth is about 4° and is frequency independent; at the ER-2 aircraft cruising altitude of about 20 km, the footprint at a typical ice cloud altitude of 10 km is 600 m. The scan cycle of CoSSIR is 4.6 s. During each scan cycle the antennas view an effective angular swath of ±50° (from nadir) for 2.6 s, as well as hot (maintained at about 328 K) and cold (at an ambient temperature of about 255 K) calibration targets for 0.5 s each. These calibration targets are closely coupled to the antennas, and their temperatures are each measured by eight resistive temperature sensors to within 0.1 K. The calibration accuracy of the CoSSIR-measured scene brightness temperatures T_b is estimated to be within ±2 K in the T_b range of 100–300 K.

Table 1 gives a comparison of the calculated and measured noise equivalent temperature difference (NEΔT) for all of the working channels; the 380.2 ± 0.8 GHz channel and the 487-GHz horizontal polarization receiver did not function during the entire deployment. Clearly the measured values of NEΔT are 2–10 times the calculated values. The excess noise is attributed to inadequate grounding and the analog-to-digital conversion. A modification to the signal conditioning and grounding is required to eliminate this excess noise source and improve the sensor performance. In addition, the local oscillator for the 380-GHz receiver exhibited instability, which prevented those channels from being used for sounding.

Table 2 lists a summary of the CoSSIR flights for this deployment. There were a total of 11 science flights in Florida and two transit flights between NASA Dryden Flight Research Center at Edwards Air Base, California, and Key West in July 2002. CoSSIR experienced a motion control problem for six science flights from 9 through 23 July, which was resolved by adjusting the gain of the motion control feedback. Toward the end of the 10th science flight on 28 July, the pilot inadvertently turned off the power to CoSSIR before descent and the whole system was cold soaked after landing. Only the four lowest frequency channels (183.3 and 220 GHz) and the 640-GHz channel remained operational after this incident. The calibrated CoSSIR datasets along nadir were placed in the CRYSTAL FACE archive (available online at http://espoarchive.nasa.gov/). The imagery datasets are deemed to be too large for archiving; they will be made available by contacting one of the authors (e.g., james.r.wang@nasa.gov).

The CRS is a new instrument operating at a 94-GHz

TABLE 2. Summary of CoSSIR science flights during CRYSTAL FACE (2002).

Flight	Date	Status	Receivers working
Transit	1 Jul	Successful	183.3, 220, 380, 487, and 640 GHz
1	3 Jul	Successful	183.3, 220, 380, and 640 GHz
2	7 Jul	Successful	183.3, 220, 380, and 640 GHz
3	9 Jul	Failed	
4	11 Jul	Failed	
5	13 Jul	Failed	
6	16 Jul	Failed	
7	19 Jul	Failed	
8	23 Jul	Failed	
9	26 Jul	Successful	183.3, 220, 380, and 640 GHz
10	28 Jul	Successful	183.3, 220, 380, and 640 GHz
11	29 Jul	Successful	183.3, 220, and 640 GHz
Transit	30 Jul	Successful	183.3, 220, and 640 GHz

frequency that was built and first flown in CRYSTAL FACE. It is a Doppler, polarimetric radar developed for autonomous operation on the ER-2 aircraft and ground operation (Li et al. 2004). Its antenna beamwidth and gain are 0.6° × 0.8° and 46.4 dB, respectively. It has a noise figure of 10.0 dB, and its receiver bandwidth can be varied between 1, 2, and 4 MHz. The system transmits power in either vertical (V) or horizontal (H) polarization and receives backscatter power in both V and H polarization at the nadir direction. The dataset that is used here has a measured sensitivity of -29 dBZe at a 10-km range, 150-m range resolution, and 1-s averaging. The calibration of the CRS was conducted by two different methods. The first one was an intercomparison of the concurrent ground-based measurements for similar cloud volumes between the CRS and the ground-based 95-GHz Cloud Profiling Radar System (CPRS) that is owned by the University of Massachusetts (Sekelsky and McIntosh 1996) and has been well maintained and calibrated over the past decade. This comparison demonstrated consistency between the two instruments to better than 1 dB (Li et al. 2004). The second method was to use the ocean surface (Durden et al. 1994) by estimating the scattering cross section of the surface return σ_0 at a low incidence angle with a quasi-specular scattering theory (Valenzuela 1978). The ER-2 aircraft dropsondes provided temperature, pressure, relative humidity, and near-surface wind conditions that were required to take into account the effect of atmospheric absorption by water vapor and oxygen, as well as the calculations of σ_0. The analysis showed that the calculated σ_0 agreed with the other CRS calibration results. The details of the system descriptions, sensitivity, and calibration can be found in Li et al. (2004). The CRS successfully collected scientific data from all of the flights listed in Table 2.

Figures 1, 2, and 3 provide a glimpse of the data acquired by the CoSSIR and CRS during CRYSTAL FACE. Figure 1 shows an example of the pseudocolor image of brightness temperatures for several selected CoSSIR channels from a segment of a transit flight
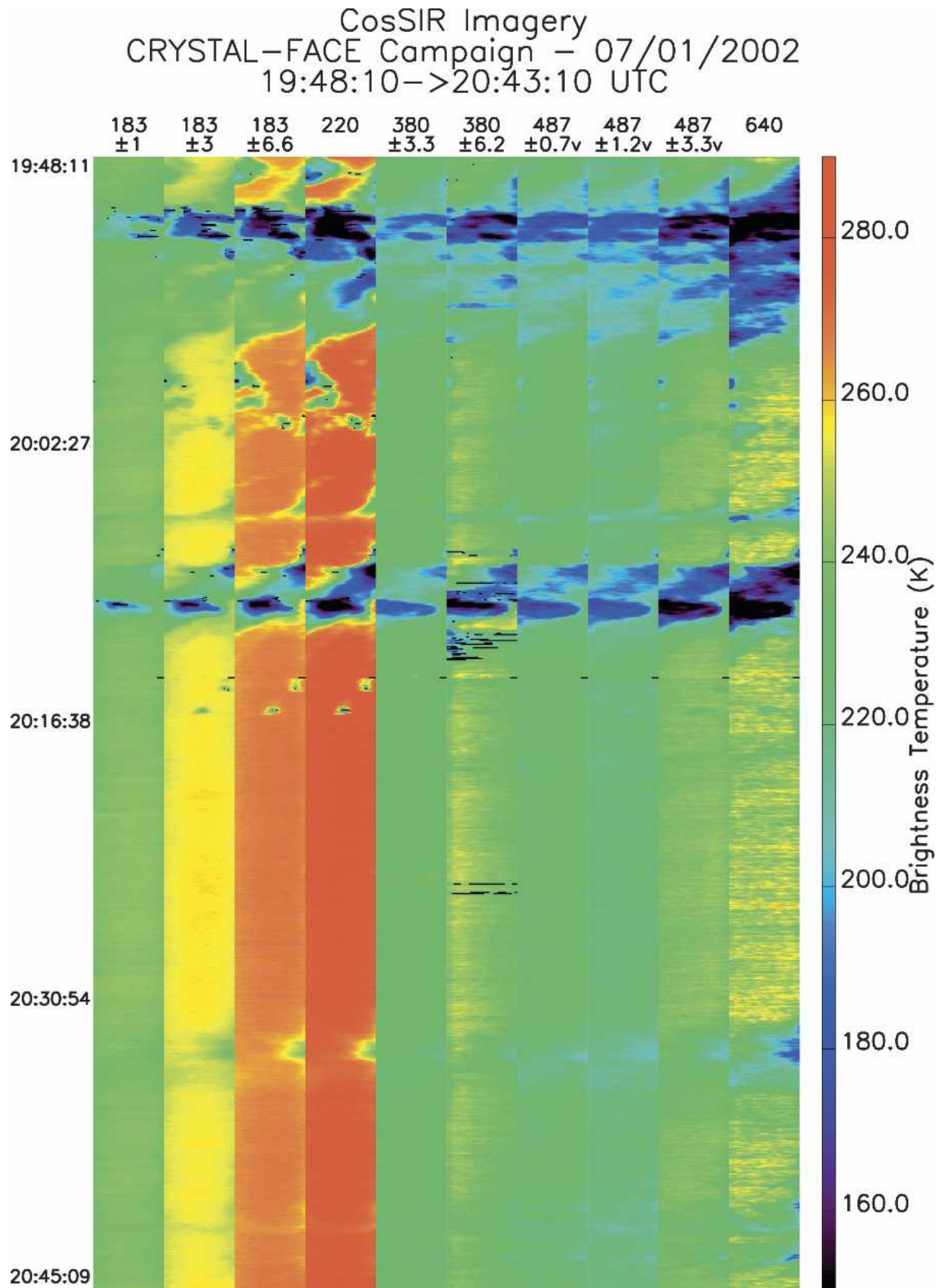
FIG. 1. Example brightness temperature images from 10 of CoSSIR's channels.
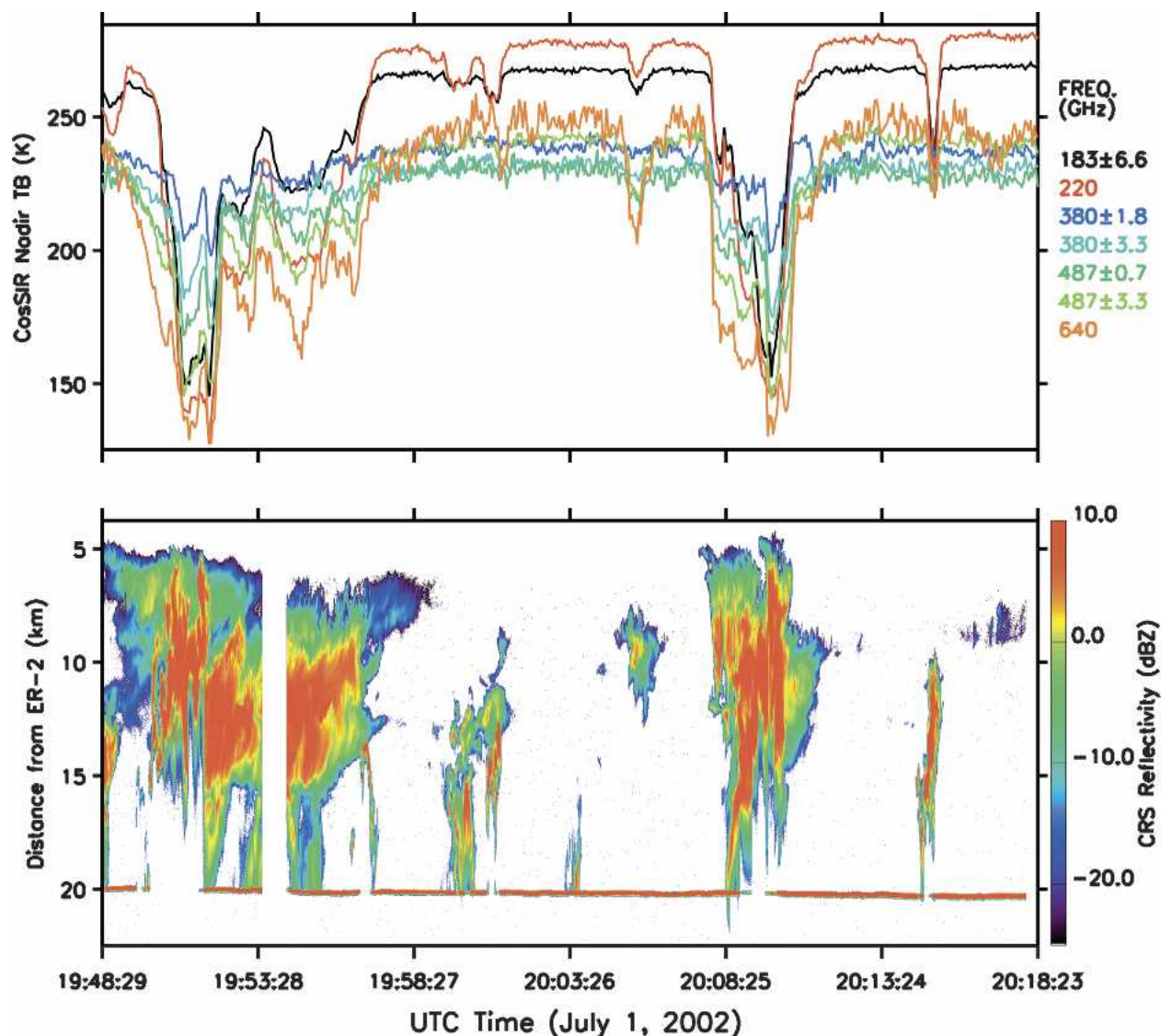
FIG. 2. (top) Nadir CoSSIR brightness temperatures and (bottom) corresponding CRS radar reflectivity.

from NASA Dryden Flight Research Center to Key West on 1 July 2002. The swath of each image is about 45 km across at the ground (much less for high clouds), and the segment covers a distance of about 600 km. Two strong cells of ice clouds can be found near the times of 1952 and 2010 UTC; a weak cell is also spotted at 2032 UTC. These cells clearly demonstrate that ice clouds strongly scatter submillimeter-wave radiation and that the T_b depressions are generally larger at higher frequencies. Notice that the effect of water vapor absorption causes a large range in the T_b values from the three 183.3-GHz channels.

Figure 2 gives a comparison of the along-nadir T_b values from some selected CoSSIR channels with the concurrent radar reflectivity profiles Z_e measured by the CRS. The time interval of the plot covers about the top half of the images in Fig. 1. The two large T_b depressions near 1952 and 2010 UTC that are identified with the ice clouds from the T_b images in Fig. 1 are clearly associated with the high CRS Z_e values. The T_b depression from the isolated high cloud around 2006 UTC is much greater at 640 than at 220 GHz. Another smaller 640-GHz T_b depression near 2016 UTC that is not apparent in Fig. 1 finds its correspondence in the CRS Z_e profile as well. Additionally, the higher-frequency channels generally show T_b depressions over a greater distance than the lower-frequency channels. For example, the T_b values around 1958 UTC from the 183.3 ± 6.6 and 220-GHz channels are already recovered to their clear-sky values, while those from the 640-GHz channel remain slightly depressed because of the presence of high clouds that are detected by the CRS.
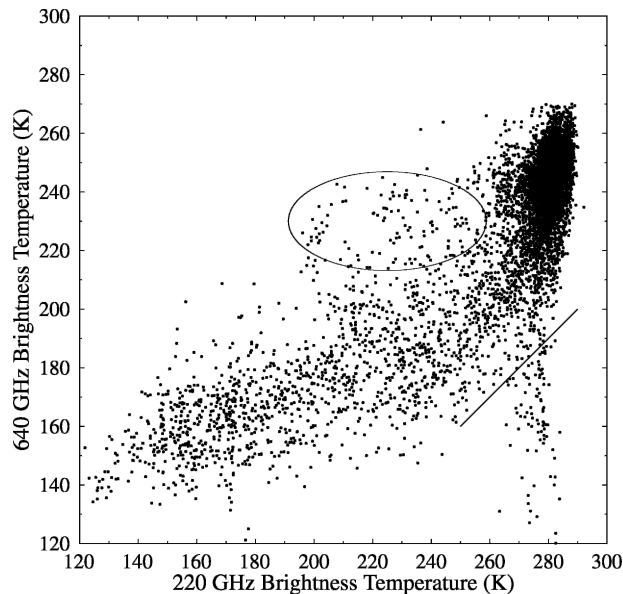
FIG. 3. Scatterplot of nadir CoSSIR 640- and 220-GHz brightness temperatures from 3, 28, and 29 Jul. See text for discussion of points delineated by the line and ellipse.

This demonstrates the increased sensitivity of the 640-GHz channel to high and thin clouds, which complements the lower-frequency sensitivity to larger particles and lower altitudes. For example, around 2000 UTC the 220-GHz channel shows a double-dip structure, while the 640-GHz channel has only the second dip. The radar profile indicates that the 640-GHz channel misses the first cell because it is at a lower altitude, where water vapor absorption blocks the 640-GHz signal.

Another important feature displayed by the CoSSIR data is the nonlinear behavior of the T_b relation between high and low frequencies, shown by the scatterplot in Fig. 3 for the 640- and 220-GHz channels. In the higher T_b range with small depressions, the 640-GHz T_b decrease is steeper than the 220-GHz decrease, implying a higher sensitivity of 640 GHz to thinner ice clouds. This higher sensitivity of the higher frequency implies clouds with smaller median mass diameter (D_{me}) particles [see Fig. 3 of Wang et al. (1998)]. In the lower T_b range, corresponding to larger depressions, the 640-GHz depression is less than that at 220 GHz, implying a larger D_{me} and generally thick clouds over regions of precipitation. The small population of points below the slanted line is from times when the 640-GHz T_bs were drifting unphysically. The points inside the ellipse are from lower-altitude ice clouds (as verified by CRS data), for which the water vapor absorption reduces the T_b depression at 640 GHz.

3. Vertically integrated ice cloud retrieval algorithm

A Monte Carlo Bayesian integration algorithm (Evans et al. 2002) is used to retrieve ice cloud IWP and

D_{me} from the CoSSIR brightness temperatures. The Monte Carlo integration is over state vectors $\mathbf{x}_i$ of cloud and atmosphere parameters. A priori information on the temperature and water vapor profile and ice cloud geometry and microphysics is introduced by distributing the vectors randomly according to a prior probability density function (pdf) $p_p(\mathbf{x})$. A radiative transfer model simulates CoSSIR brightness temperatures $T_{\text{sim},j}$ (for the jth channel) from the cloud and atmosphere profile represented by $\mathbf{x}_i$. A retrieval for the CoSSIR-observed brightness temperatures $T_{\text{obs},j}$ (with rms uncertainty of σ_j) is performed by computing the mean state vector over the posterior pdf from the Bayes theorem. Assuming a normally distributed likelihood function for the observations given the state vector, the retrieved state is

$$\mathbf{x}_{\text{ret}} = \frac{\sum_i \mathbf{x}_i \exp\left(-\frac{1}{2}\chi_i^2\right)}{\sum_i \exp\left(-\frac{1}{2}\chi_i^2\right)} \quad \mathbf{x}_i \text{ from } p_p(\mathbf{x}), \quad (1)$$

where χ^2 is the usual normalized measure of the disagreement between the observed and simulated brightness temperature vectors

$$\chi_i^2 = \sum_{j=1}^M \frac{[T_{\text{obs},j} - T_{\text{sim},j}(\mathbf{x}_i)]^2}{\sigma_j^2}. \quad (2)$$

An estimate of the uncertainty in the retrieval is given by the standard deviation around the mean vector,

$$\sigma_x^2 = \frac{\sum_i (\mathbf{x}_i - \mathbf{x}_{\text{ret}})^2 \exp\left(-\frac{1}{2}\chi_i^2\right)}{\sum_i \exp\left(-\frac{1}{2}\chi_i^2\right)} \quad \mathbf{x}_i \text{ from } p_p(\mathbf{x}). \quad (3)$$

For efficiency, the simulated brightness temperatures for each Monte Carlo vector ($\mathbf{x}_i$) are precomputed with a radiative transfer model and stored with the desired retrieval parameters (e.g., IWP and D_{me}) in a file called the retrieval database. The database used here has 10^6 cases in it.

Several minor improvements have been made to the Bayesian ice cloud retrieval algorithm that is described in Evans et al. (2002). Missing channels are dealt with by simply setting that channel's σ_j to 1000 times the normal value. The algorithm requires a minimum number of database points (25 in the retrievals below) within a specified χ^2 threshold, here set to $M + 4\sqrt{M}$, where M is the number of channels in the retrieval. This choice of the χ^2 threshold is guided by noting that for Gaussian measurement noise and $M \gg 1$, the expected value of χ^2 is M and the standard deviation of χ^2 is $\sqrt{2M}$. If there are fewer than the required number of points within this threshold because of the finite num-

ber of points in the retrieval database, then a larger χ^2 range is considered by effectively increasing all of the σ_js in steps of a factor of $\sqrt{2}$ until the minimum number of points is reached. This implies that there is a source of retrieval error due to the finite database size. Because the points in the database are distributed according to the prior pdf, there are few cases with a high IWP. The database-generation procedure has the option of rejecting low IWP cases according to an exponential probability distribution in IWP and increasing the weight of the remaining cases so that the high IWP–enriched retrieval database is statistically equivalent to the prior pdf. This procedure improves the problem of not having enough database points within the required χ^2 threshold for higher IWP.

Generation of the database of atmospheric parameters and corresponding brightness temperatures is the key element of the Bayesian algorithm. The first step in generating the database is to create random profiles of temperature, water vapor, liquid and ice cloud properties, and surface emissivity. The distribution of these parameters is the a priori information in the retrieval, and so it is important that the profiles are realistic and that they completely cover the possible parameter range. The retrieval does depend on the prior distribution, but the variation in the retrieved parameters due to the a priori assumptions is small relative to the retrieved error bars (as long as the prior distribution contains a wide range of atmospheric states and the measurements provide useful information).

The retrieval database temperature and relative humidity profiles are generated with appropriate statistics and vertical correlations using the principal component analysis. The principal components are calculated from 25 radiosonde profiles on 3, 7, 9, 21, 28, and 29 July, obtained from the Miami National Weather Service and the Pacific Northwest National Laboratory (PNNL) Atmospheric Remote Sensing Laboratory (PARSL) at the West Coast ground site. Twenty principal components, which explain 99.8% of the variance in temperature and relative humidity, are used. Heights above the highest radiosonde level and the fixed ozone profile are obtained from a standard tropical atmosphere. The mean relative humidity profile in the generation process (not the output stochastic profile) is set to ice saturation for the cloudy levels.

This retrieval database is made with single-layer clouds, which may be ice, mixed phase, or even pure liquid, depending (stochastically) on temperature. The cloud geometry statistics are obtained from over 1400 cloudy CRS profiles on four flights, where the thickest cloud layer with a top height above 9.5 km is chosen from each profile. The top height is Gaussian distributed with a mean of 12.7 km and a standard deviation of 1.2 km. The cloud thickness is exponentially distributed with a mean of 5.0 km.

The microphysical properties of the ice clouds in the retrieval database are based on CRYSTAL FACE data from in situ cloud probes on the Citation aircraft. The results of this analysis (described in appendix A) are the joint statistics of temperature, IWC, and D_{me} as summarized by the mean vector and covariance matrix of temperature, ln(IWC), and ln(D_{me}). The randomly generated ice cloud heights and thicknesses are used to index into the random temperature profiles to get cloud-top and -bottom temperatures. Given the top and bottom temperature, the IWC and D_{me} at the top and bottom of the cloud are generated randomly from the bivariate lognormal distribution. The D_{me} varies linearly with height inside the cloud, while the IWC varies as a power law in D_{me}. The bottom IWC and D_{me} are required to be larger than the cloud-top values.

Ice particle shape and size distribution width are error sources in the ice cloud retrievals. The construction of random aggregate particles, based loosely on Cloud Particle Imager pictures and the simulation of CoSSIR and CRS scattering properties for size distributions of these particles, is described in appendix B. For each cloud a single particle shape is selected from the five modeled shapes (low-density spherical snow, aggregates of frozen droplets, two varieties of aggregates of hexagonal plates, and aggregates of plates and hexagonal columns). The width of the ice particle gamma-sized distribution is also randomly chosen for each cloud from three widths.

The surface has a small contribution at 220 GHz for the drier stochastic atmospheres (the 220-GHz transmission for the mean atmosphere is only 4.4%). Even the driest atmospheres have essentially no transmission at the other CoSSIR frequencies. The surface emissivity is Gaussian distributed with a mean of 0.93 and a standard deviation of 0.03 (representing a land surface). The surface temperature is obtained from the random atmosphere temperature at zero height.

The second part of generating the retrieval database is to simulate the CoSSIR and CRS observations with a radiative transfer model. A fast Eddington second approximation method is used. The microwave radiances are simulated for a nadir-viewing angle. For efficiency, the monochromatic absorption profiles for an input atmosphere are interpolated in temperature and water vapor from reference profiles that are calculated with the Line-by-Line Radiative Transfer Model (LBLRTM), version 8.3. Double-sideband brightness temperatures are calculated with two monochromatic radiative transfer computations. The tabulated single scattering properties for the ice particles are computed as described in appendix B.

In addition to the simulated CoSSIR brightness temperatures, the retrieval database has two simulated 94-GHz CRS observables—integrated attenuated backscattering (I_b) and the mean backscattering weighted height (z_b). The integrated attenuated backscattering is defined by

TABLE 3. CoSSIR channels and brightness temperature uncertainties (σ_j, K) used in retrievals.

Day	Channels (GHz)						
	183.3 ± 1.0	183.3 ± 3.0	183.3 ± 6.6	220.0	380.2 ± 6.2	487.2 ± 3.0	640
1	2.0	2.0	2.0	1.5	8.0	7.0	7.0
3	2.0	2.0	2.0	1.5	10.0	—	6.0
7	2.0	2.0	2.0	1.5	10.0	—	16.0
28	2.0	2.0	2.0	1.5	7.0	—	10.0
29	2.0	2.0	2.0	1.5	—	—	12.0
30	2.0	2.0	2.0	1.5	—	—	12.0

$$I_b = \int_{z_1}^{z_2} \frac{\sigma_{\text{back}}(z)}{4\pi} e^{-2\tau(z)} \, dz = \int_{z_1}^{z_2} \frac{\sigma_{\text{sca}} P(180°)}{4\pi} e^{-2\tau(z)} \, dz,$$

(4)

and the mean backscattering weighted height is defined by

$$z_b = \frac{\int_{z_1}^{z_2} \sigma_{\text{back}}(z) z e^{-2\tau(z)} \, dz}{\int_{z_1}^{z_2} \sigma_{\text{back}}(z) e^{-2\tau(z)} \, dz},$$

(5)

where $\sigma_{\text{back}}(z)$ is the volume backscattering coefficient, σ_{sca} is the volume scattering coefficient, $P(180°)$ is the phase function evaluated in the backscattering direction, $e^{-2\tau(z)}$ is the two-way attenuation along the optical path $\tau(z)$, and $z_1 – z_2$ is the height range. The height range used here is 4.5–17 km, or all cloudy levels above the freezing level. Although not in common use in radar meteorology, integrated backscattering is a natural measure in radiative transfer and is used in lidar remote sensing. The units of integrated backscattering are per steradian. The radar observables in the database are used 1) to retrieve I_b from CoSSIR data to compare with CRS data and 2) to perform IWP and D_{me} retrievals with the combination of CoSSIR and CRS data.

4. CoSSIR and CRS vertically integrated ice cloud retrievals and analysis

To perform the Bayesian ice cloud retrievals from CoSSIR measurements, the rms uncertainties (σ_j) must be determined for each channel during each flight. Only the nadir-viewing CoSSIR brightness temperatures for roll angles less than 8° are used. The "noise" of the CoSSIR T_bs are determined by calculating the standard deviation for clear-sky segments of the flights. Here clear sky is defined as those pixels for which the MODIS Airborne Simulator (MAS) 11.0-μm brightness temperature is above 295 K. This method for estimating σ assumes that most of the variability is instrumental and is not due to water vapor variability, which is true for the channels above 220 GHz. The variability estimate is probably high for the 183- and 220-GHz channels. The actual σ that is used is chosen somewhat

subjectively between the standard deviations for short time segments and those for the whole flight. The channels and σ used in the retrievals are listed in Table 3 for each flight. These T_b uncertainties are larger than those in Table 1 because the measured NEΔTs were calculated from calibration target looks and do not include other sources of uncertainty, such as noise spikes from the scanning mechanism and calibration drifts. The σ for the 183- and 220-GHz channels are kept fixed, while those for the other channels vary with the flight. To minimize the error due to uncertainties in the exact local oscillator frequency for the 380- and 487-GHz receivers, we use only the channel with the bandpass that is farthest from the central frequency.

The evaluation of CoSSIR IWP and D_{me} retrievals is carried out by comparing integrated attenuated reflectivity retrieved from CoSSIR with that calculated from the CRS data. This indirect approach avoids the large errors in retrieving IWP and D_{me} from radar reflectivity profiles. The CRS data are relatively independent of the CoSSIR T_bs, because the CRS reflectivity is backscattering and is at a considerably lower frequency.

Figure 4 illustrates this idea of independent physics by comparing the sensitivity to the particle size of CRS reflectivity and CoSSIR brightness temperature depressions for a fixed ice water content. A particle size exponent n near zero means that the measurement is related to IWP with little dependence on D_{me}. For smaller particles the CRS reflectivity is in the Rayleigh regime, where $n \approx 3$, but the exponent decreases for larger particles as 94 GHz enters the Mie regime. A negative exponent means that the ΔT_b decreases with increasing particle size for a fixed ice mass (the geometric optics limit has $n = -1$). The large difference in the D_{me} exponents between the CRS and various CoSSIR channels implies that the CRS and CoSSIR are independent measurements over most of the range in D_{me}.

The comparison of CoSSIR retrievals with CRS data is limited to flights on 3, 7, 28, and 29 July. The CoSSIR retrievals for 1 and 30 July are only strictly valid for the end or the beginning of the flights when the ER-2 was in the south Florida vicinity (prior information on the atmospheric profile, and perhaps the microphysics, is expected to change with location). For comparison with CoSSIR retrievals and to use in combined retrievals,
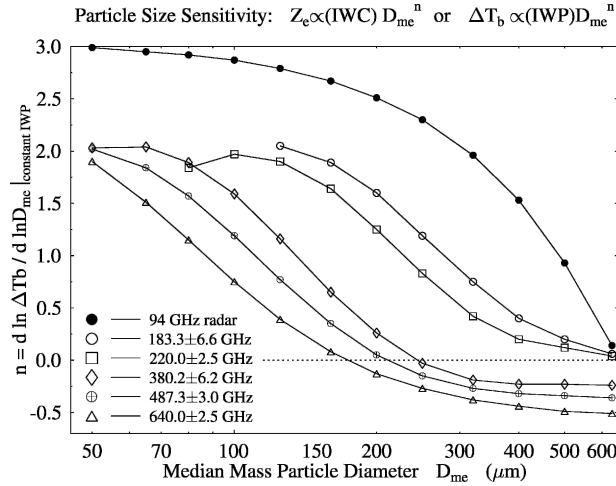
Particle Size Sensitivity: $Z_e \propto$(IWC) D_{me}^{n} or $\Delta T_b \propto$(IWP)D_{me}^{n}

FIG. 4. Theoretical calculations comparing the sensitivity to particle size (D_{me}) for constant IWC of 94-GHz radar reflectivity (Z_e) and CoSSIR brightness temperature depressions (ΔT_b). The ice water content is 0.1 g m^{-3} and the cloud is from 9 to 12 km, giving an IWP of 300 g m^{-2}. The ice particles are sphere aggregates (see appendix B), and a Miami sounding from 28 Jul is used. Only those particle sizes having $\Delta T_b > 1.0$ K are shown.

the CRS data are vertically averaged and converted to integrated attenuated backscattering, using

$$I_b = \int \frac{\pi^4 |K_w|^2}{4\lambda^4} Z_e \, dz$$

$$= (1.653 \times 10^{-7} \text{ m}^2 \text{ mm}^{-6}) \int Z_e \, dz, \qquad (6)$$

where $|K_w|^2 = 0.6975$, $\lambda = 0.3184$ cm is the wavelength, Z_e is the CRS equivalent radar reflectivity factor, and the integration is from 4.5 to 17 km. The integrated backscattering (with units of per steradian) is converted to decibels. As an example, a 10-km-deep cloud with a CRS reflectivity of 10 dBZe has an integrated backscattering of −17.8 dB. The mean and standard deviation of integrated backscattering for no-echo conditions is −58.5 and 2.75 dB, respectively. Therefore −50 dB is taken as the threshold for using integrated backscattering data in the analysis below.

Figure 5 shows an example of CoSSIR IWP and D_{me} retrievals and a comparison of CoSSIR-retrieved and CRS-integrated backscattering. The IWP ranges up to over 10 000 g m^{-2} for the thickest parts of the anvils. The retrieved IWP error is approximately equal to the IWP for IWP below about 200 g m^{-2}. The reason for the poor sensitivity to low IWP is the high noise on the more sensitive submillimeter channels (380 and 640 GHz; see Table 3). The retrieved D_{me} ranges from 500–600 μm in the thickest regions to around 200 μm (though with large error bars) in the thin anvil regions. There is remarkable agreement between the retrieved and CRS-integrated backscattering in the thick anvil
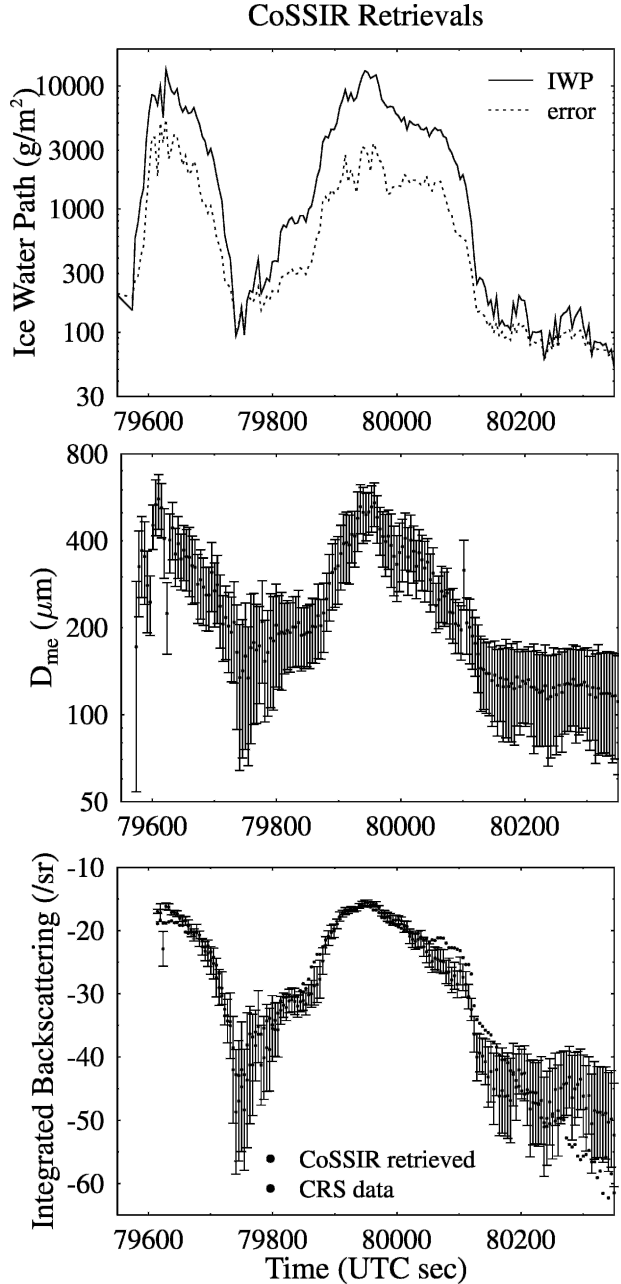

FIG. 5. Example retrievals (with 1 σ errors) of (top) ice water path, (middle) D_{me}, and (bottom) integrated backscattering from CoSSIR brightness temperatures on 28 Jul.

regions. The retrieved integrated backscattering error bars are also very small for the deep anvils. In the thinner regions the integrated backscattering error bars increase substantially, and, thus, the retrievals still agree statistically with the CRS data.

Statistics comparing the retrieved and CRS-integrated backscattering are shown in Fig. 6 for the 1027, 2814, 1050, and 1225 retrievals on July 3, 7, 28, and 29, respectively. For all of the four flights the median dif-
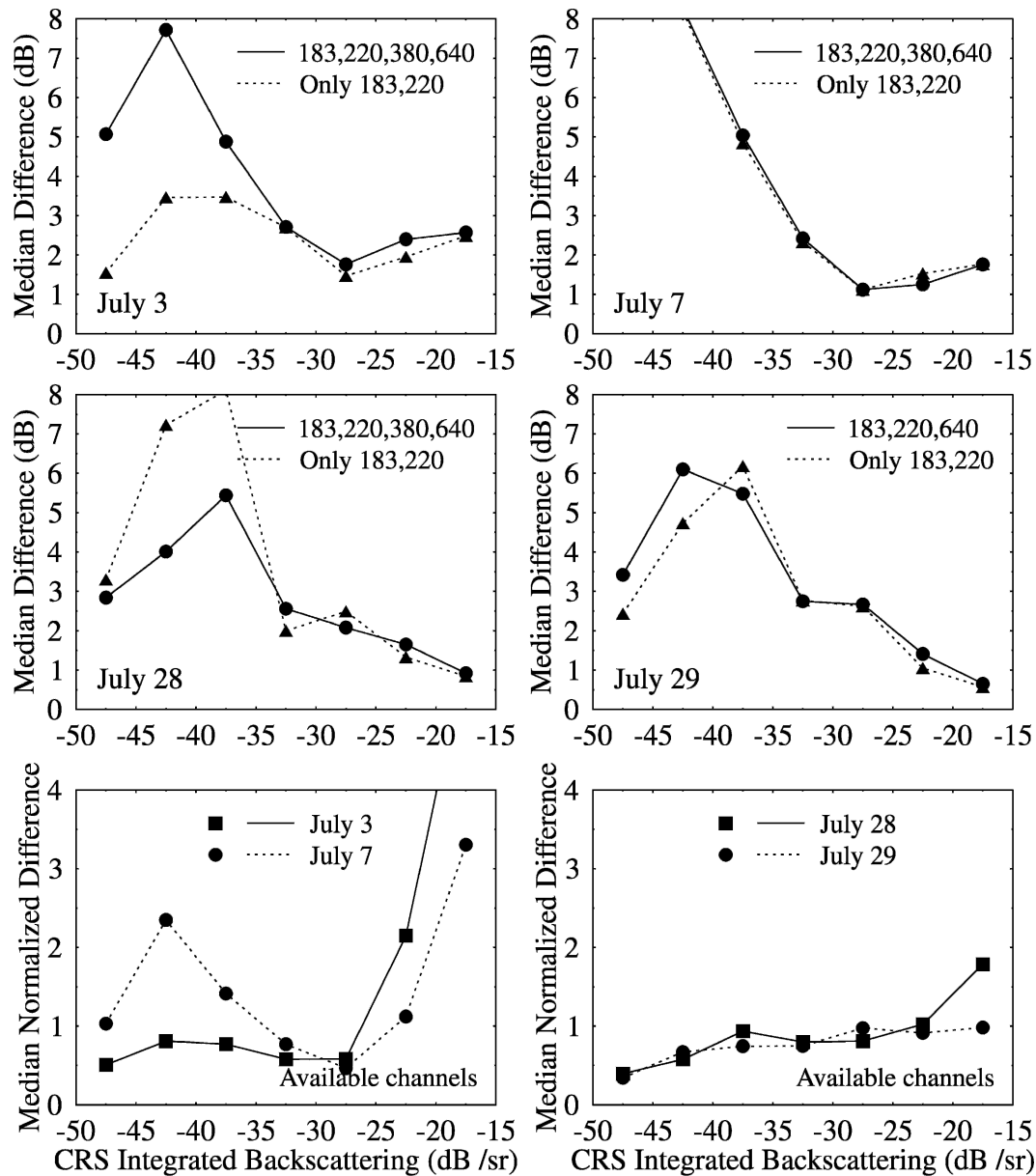
FIG. 6. The top four graphs show the median absolute difference between CoSSIR retrieved and CRS integrated backscattering as a function of CRS integrated backscattering (in 5-dB-wide bins). The bottom two graphs show the median absolute normalized difference, where the normalization is by the retrieved integrated backscattering error.

ferences are below 3 dB for integrated backscattering above −35 dB. For the 28 and 29 July flights the differences drop to 1 dB or below for the highest integrated backscattering (from −20 to −15 dB), but the retrieval error for the 3 and 7 July flights is somewhat larger. In addition to the CoSSIR retrieval, using the channels listed in Table 3, the integrated backscattering error statistics are also shown for retrievals using just the three 183- and one 220-GHz channels. Eliminating the submillimeter channels slightly degrades the thinner region retrievals on 28 July but dramatically *im-*

proves the thinner region retrievals on 3 July. This may indicate that the submillimeter channels were malfunctioning on 3 July, or that the CoSSIR T_b errors are underestimated. On 7 July, the integrated backscattering retrieval errors with and without the submillimeter channels are almost the same, presumably because of the large uncertainties for the submillimeter channels on that flight. The lack of a significant improvement in the integrated backscattering retrieval error for thinner anvil regions with the addition of the submillimeter channels is another indication that those channels were

too noisy to add much value to the low-noise millimeter-wave channels.

Another measure of the integrated backscattering retrieval error is the normalized differences shown in Fig. 6, which are the median of the absolute value of the integrated backscattering differences divided by the retrieved error bars. The normalized differences are generally about unity or less, except for the high-radar-reflectivity regions on 3 and 7 July. This suggests that the Bayesian error bars are reasonably estimated and that there are no large systematic errors in the retrievals, except perhaps in the deep precipitating regions on 3 and 7 July.

In addition to using the CRS-integrated backscattering to evaluate the CoSSIR retrievals, it can also be input to the Bayesian retrieval algorithm. In this case, there is no longer any validation, but it is still useful to see how the IWP and D_{me} retrievals, and especially the error bars, behave. In addition to the integrated backscattering, the backscattering-weighted cloud height is input to the Bayesian algorithm. The calibration uncertainty (σ) in CRS-integrated backscattering that is used for the retrieval is 1.0 dB, and the σ for the weighted cloud height is taken to be 0.5 km (so as to not unnecessarily restrict the number of matching database cases). The retrieval results for 28 July are presented here statistically in Fig. 7, which shows the median retrieved IWP and D_{me} as a function of integrated backscattering for CRS-only, CoSSIR-only, and CRS + CoSSIR retrievals. Overall, the retrievals for the three instrument configurations are fairly similar. In the thickest anvil regions the CRS-only-retrieved IWP is smaller than when CoSSIR data are included. The retrieved IWP errors are smaller for CoSSIR-only than for CRS-only retrievals, and decrease further with their combined retrievals. The D_{me} errors for the lowest integrated backscattering bin are actually larger for CoSSIR-only than for CRS-only retrievals, because CoSSIR with the noisy submillimeter channels lacks any sensitivity there. Except for the low-reflectivity regions, the D_{me} errors are much lower for the combination of CRS and CoSSIR than for CRS data alone.

5. CRS and CoSSIR profile retrievals

A new algorithm was devised to retrieve profiles of IWC and D_{me} from the combination of CRS radar reflectivity profiles and CoSSIR brightness temperatures. The major assumption of the method is that the ice water content profile is related to the reflectivity profile by IWC $= 10^{0.1p}Z_e^q$. However, the coefficients p and q are retrieved for each column from the combined CRS and CoSSIR data in a Bayesian procedure.

The a priori probability distribution of p and q is assumed to be a bivariate Gaussian distribution. The parameters of this distribution (mean and standard deviation of p and q and the correlation between them) is
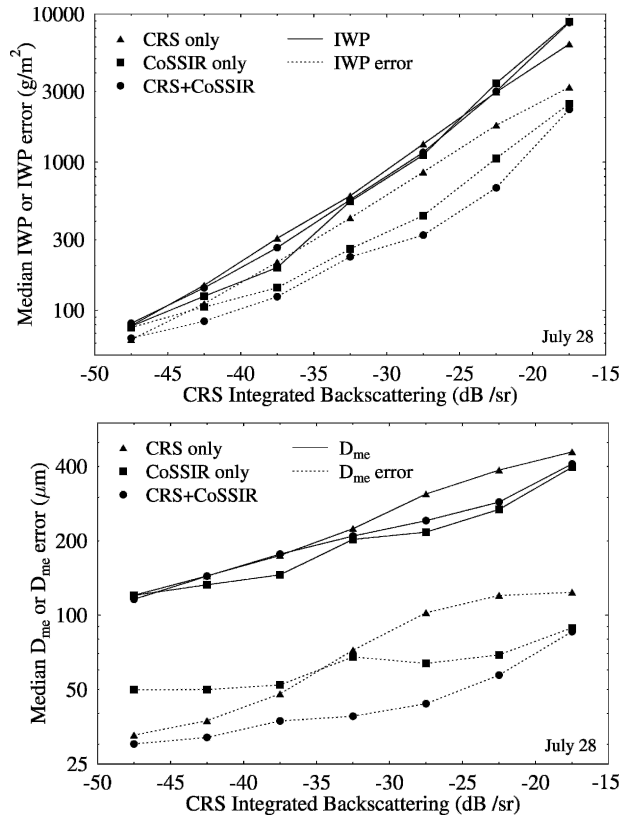

FIG. 7. Median retrieved (top) IWP and (bottom) D_{me}, and errors for three combinations of CRS and CoSSIR data plotted against integrated CRS backscattering (for 5-dB-wide bins).

obtained from a Monte Carlo simulation using the same microphysical statistics used in the vertically integrated Bayesian retrieval. The IWC and D_{me} in each of the six uniform layers from 4.5 to 15.5 km is obtained by random sampling the bivariate normal distribution of ln(IWC) and ln(D_{me}) given the temperature of that layer. A random scattering table (i.e., a particular particle shape and gamma distribution width) containing the D_{me} is chosen for each layer. The radar reflectivity Z_e for a layer is calculated from the IWC and D_{me} using the scattering table. A linear regression of 10 $\log_{10}$(IWC) against 10 $\log_{10}(Z_e)$ then gives the p and q coefficients for that randomly sampled profile. This process is carried out for 100 000 random profiles to obtain the prior pdf of p and q. The means of p and q are -7.114 and 0.488, the standard deviations of p and q are 1.742 and 0.112, and the correlation between p and q is 0.472. The assumption of six independent uniform layers is fairly arbitrary, of course; the standard deviations of p and q decrease predictably as the number of independent layers increase.

A profile retrieval is performed with a Monte Carlo integration over the Bayes theorem posterior pdf. First a threshold is applied to the radar profile to remove noisy pixels (using -30 dBZ at a 5-km range), and the

profile is averaged to the desired vertical resolution over the range (0.25 km from 4.5 to 15.5 km here). The CoSSIR data are merged by interpolation to the CRS time if they are within 3 s. For each sample point in the Bayesian integration, a random p and q from the a priori distribution are chosen. A random Gaussian-distributed 1.0-dB rms offset is added to the reflectivity profile (dBZ) to simulate calibration uncertainty, and the corresponding IWC profile is calculated from the reflectivity profile using p and q. A scattering table (with one particle shape and gamma distribution width) is chosen randomly for the profile. For each level in the profile the scattering table is used to find a D_{me} corresponding to the IWC and radar reflectivity Z_e. Along with the microphysical profile, a random temperature and humidity profile is made using the same technique previously described (in section 3). The fast radiative transfer method (section 3) is then used to simulate the CoSSIR T_bs from the profile, and, hence, compute the χ^2 measure of proximity to the observed T_bs. The retrieved IWC and D_{me} profiles and p and q are the mean over the random sample points that are weighted by the likelihood function, $\exp(-\chi^2/2)$. The retrieved error bars are the posterior-weighted standard deviation over the integration points. The Bayesian integration loops over a maximum number of random samples (10 000 here), but, to save time, quits early if enough samples with low χ^2 are obtained (e.g., 400 with $\chi^2 < M + 3\sqrt{2M}$ for M CoSSIR channels). The profile-retrieving algorithm assumes negligible attenuation of the 94-GHz radar down to 4.5 km. The reflectivity profile input to the method is already corrected for molecular absorption, but in the thicker anvil regions the reflectivity also attenuates from particle scattering. An improved algorithm could correct the reflectivity profile by computing the attenuation from a first-pass retrieval using the uncorrected profile.

The CRS and CoSSIR profile retrieval algorithm is run for all of the valid radar profiles on 3, 7, 28, and 29 July, using the same CoSSIR channels and σs as in section 4. The same 15 ice particle scattering tables described in appendix B are used. Figure 8 shows an example of the retrieved IWC and D_{me} profiles. The minor striping seen in the images is due to the relatively small number of points in the Bayesian integration. The retrieved IWC and D_{me} are not completely correlated as with a standard IWC–Z_e relation, as illustrated by the largest D_{me} that is on the left side of the anvil while the highest IWC is on the right side.

In addition to the profiles, the algorithm also retrieves the coefficients of the IWC–Z_e relation (p and q) and their errors. Figure 9 plots the median p and q and errors as a function of the CRS-integrated backscattering. The mean and standard deviation of the retrieved coefficients is nearly the same as that of the prior distribution when the integrated backscattering is below -35 dB. Presumably this is a result of the CoSSIR sensitivity being too low to affect the retriev-

als, which are effectively only from the CRS in the thin anvil regions. At higher integrated backscattering values, both the p and q coefficients increase away from the prior distribution mean and their uncertainties decrease. In the highest integrated backscattering bin, for example, the median coefficients are $p = -5.72$ and $q = 0.579$, which give a 70% higher IWC for $Z_e = 10$ mm^6 m^{-3} than the a priori values (1.02 versus 0.60 g m^{-3}).

6. Conclusions

The Compact Scanning Submillimeter Imaging Radiometer first flew in July 2002 during CRYSTAL FACE. Scanning across track, CoSSIR measured brightness temperatures in 12 channels with receivers at 183, 220, 380, 487, and 640 GHz. Although the submillimeter-wave channels were noisier than anticipated, the CoSSIR data demonstrate the high sensitivity of the submillimeter channels to ice cloud particles as compared with the lower frequencies. A Bayesian algorithm is used to retrieve the ice water path (IWP) and median volume equivalent sphere diameter (D_{me}) from the available CoSSIR nadir brightness temperatures. Prior information that is used by the algorithm is obtained from radiosondes and in situ cloud microphysical probes on the Citation aircraft that was flown in CRYSTAL FACE. The retrievals are tested by retrieving vertically integrated 94-GHz radar backscattering from the CoSSIR data, which is then compared to Cloud Radar System (CRS) data. The integrated backscattering typically agrees to 1–2 dB for IWP from 1000 to 10 000 g m^{-2}, while for lower IWP the typical agreement is 3–5 dB, which is within the Bayesian error bars. Retrievals of integrated backscattering using only the 183- and 220-GHz CoSSIR channels have an agreement that is almost as good because of the high noise on the submillimeter channels.

An algorithm was developed to retrieve profiles of ice water content (IWC) and D_{me} from the combination of CRS reflectivity profiles and CoSSIR brightness temperatures. A power-law relation (IWC $= 10^{0.1p}Z_e^q$) is assumed between IWC and equivalent radar reflectivity (Z_e), but the p and q coefficients are retrieved for each column. The IWC and D_{me} profiles and p and q are retrieved in a Bayesian integration that effectively matches the simulated and observed CoSSIR brightness temperatures. The radiometer data add additional information to the radar profile, so that the retrieved IWC and D_{me} are no longer completely dependent, as they are with a traditional IWC–Z_e relation. The median retrieved p and q over all of the flights both increase from the a priori values for the highest IWP clouds. The results from the combined radar–radiometer profile algorithm illustrate how the coefficients for radar-only ice cloud retrieval methods could be tuned for particular cloud types using submillimeter radiometer data.
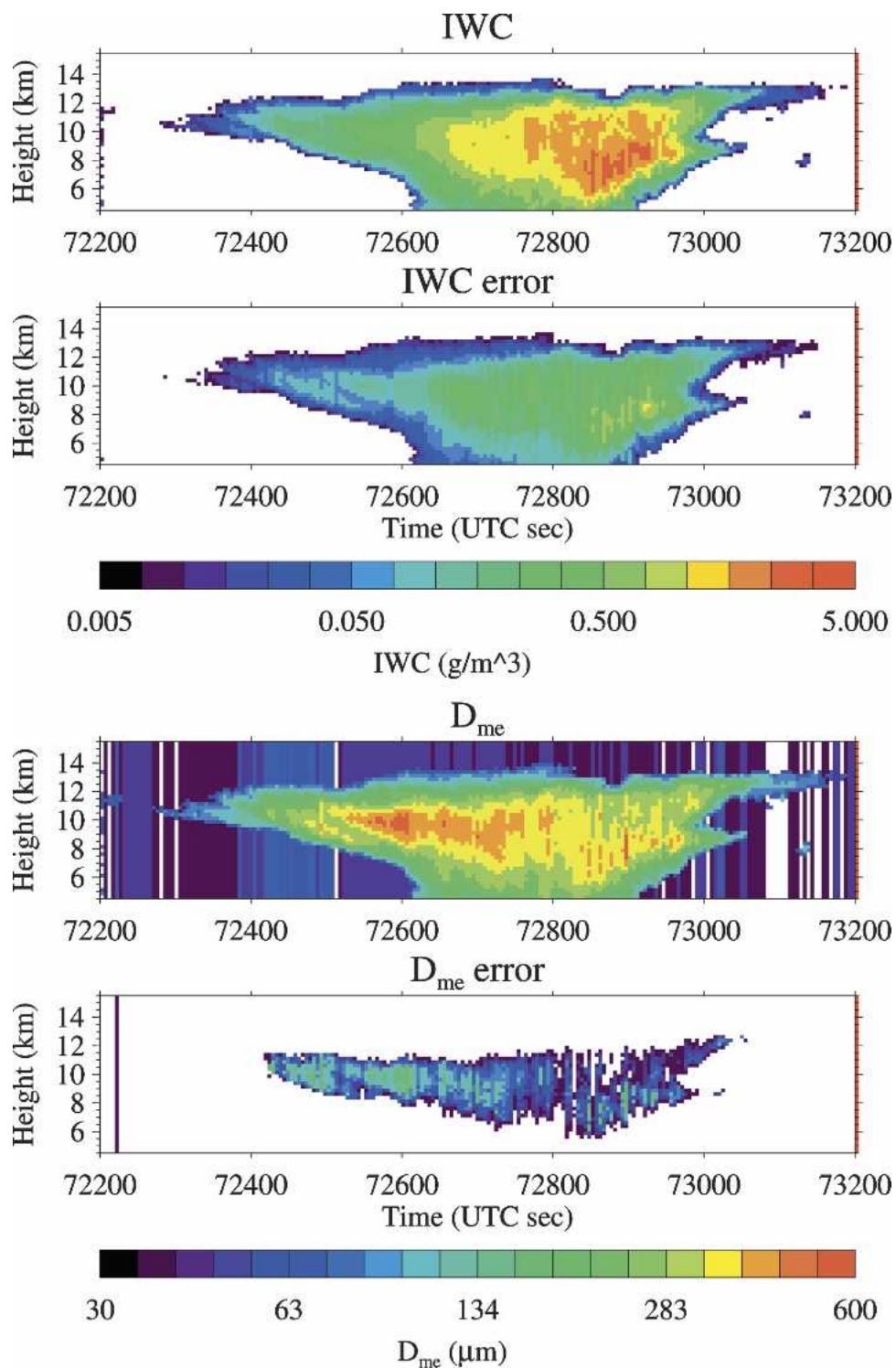
FIG. 8. Example IWC, IWC error, D_{me}, and D_{me} error fields from the Bayesian CRS and CoSSIR profile retrieval algorithm for 29 Jul.

The CoSSIR-only retrievals of IWP and D_{me}, and the combined CoSSIR and CRS retrievals of profiles of IWC and D_{me}, are available in the CRYSTAL FACE archive (online at http://espoarchive.nasa.gov/). During CRYSTAL FACE the sensitivity of CoSSIR to lower IWP clouds was much poorer than anticipated because of the high noise of the submillimeter-wave channels. CoSSIR is currently being upgraded to improve the
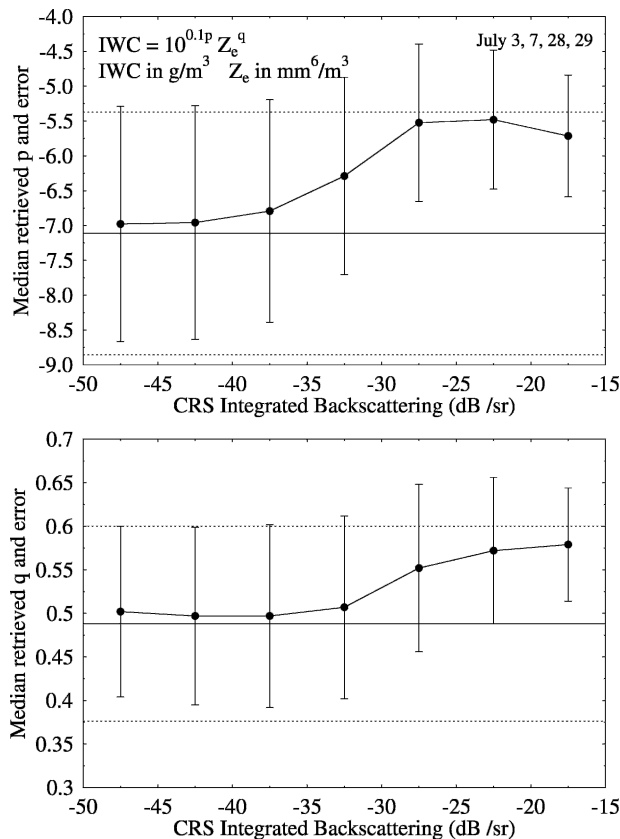
FIG. 9. Median retrieved (top) p and (bottom) q and median errors over all flights for the CRS + CoSSIR profile retrieval algorithm. The p and q are coefficients in the power-law ice water content–radar reflectivity relationship. The solid horizontal lines show the a priori mean values of p and q, while the dotted lines show ± one standard deviation.

performance of the 380-, 487-, and 640-GHz receivers to noise equivalent temperatures of better than 1.0 K. The CoSSIR upgrade will also include the addition of a 874-GHz receiver for improved sensitivity to cirrus with smaller ice particle size.

APPENDIX A

A Particle Size Distribution Analysis

The Bayesian ice cloud retrieval algorithm requires statistics on the relationship between temperature, IWC, and D_{me}. For CRYSTAL FACE the best source of these microphysical statistics are the optical cloud probes on the University of North Dakota Citation aircraft. The Citation flew at a range of lower altitudes relative to the WB-57 aircraft and thus is more representative of the microphysics that are relevant for vertically integrated retrievals. Cloud probes that measure the particle size distribution are needed to calculate the D_{me} for each sample. To cover the full range of ice particle sizes, data from the following three probes are used: the Particle Measuring Systems (PMS), Inc., Forward Scattering Spectrometer Probe (FSSP), the PMS 2D-C imaging probe, and the Stratton Park Engineering Company (SPEC), Inc., High Volume Particle Spectrometer (HVPS). The two-dimensional cloud (2D-C) probe has a 33-μm resolution, sizes up to 1000 μm, and samples about 0.007 $m^3 s^{-1}$. The HVPS probe has a 200-μm resolution, sizes up to 6000 μm, and samples about 1 $m^3 s^{-1}$. The FSSP measures size distributions from about 4 to 62 μm and is the only source that is available for the smaller ice crystals, though the concentrations tend to be overestimated because of large particle breakup and the assumption of particle sphericity.

The composite 2D-C–HVPS size distributions and the FSSP size distributions that are available from the CRYSTAL FACE data archive are analyzed in a technique similar to that in Heymsfield et al. (2004). A particle mass–maximum diameter relation of the form $m = g_0 D^{g_1}$ is assumed, and the coefficients g_0 and g_1 are adjusted to match the IWC measured by the counterflow virtual impactor (CVI) (Twohy et al. 1997). The first step is to average and merge the archived temperature, CVI IWC, and FSSP data to the 5-s samples of the 2D-C–HVPS size distributions for all of the CRYSTAL FACE Citation flights. The particle mass for each bin in a measured size distribution may be obtained from the central maximum diameter using the mass–diameter relation for a given g_0 and g_1. The IWC is then simply the sum over the bins of the particle mass times the number concentration. The procedure for determining the best fitting coefficients has two steps. The first is to try a fixed g_1 and adjust g_0 so that the median (over all samples) of the ratio R of the computed IWC to the CVI IWC is unity. The coefficient g_1 is then determined by adjusting it to minimize the ratio R_{75}/R_{25}, where R_{25} and R_{75} are the 25th and 75th percentiles, respectively, of the ratio R. The first step assures an unbiased fit, while the second step minimizes the dispersion of the optical probe IWC around the CVI IWC. We expect that using percentiles is more robust to errors, such as the CVI hysteresis. This procedure is carried out only
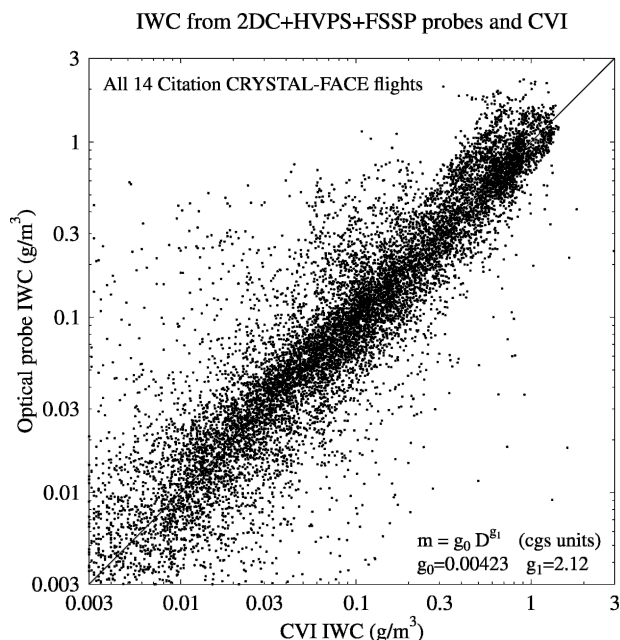
IWC from 2DC+HVPS+FSSP probes and CVI

FIG. A1. Comparison of the IWC calculated from the optical probe size distributions using the best-fitting mass–diameter relation with the CVI IWC.

for samples above the nominal CVI sensitivity of 0.01 g m^{-3} and for temperatures below −5°C. The best-fitting mass–diameter coefficients from this procedure are g_0 = 0.004 23 and g_1 = 2.12 in cgs units. Figure A1 shows a scatterplot of the resulting optical probe and CVI IWC. These coefficients give a somewhat lower IWC than those in Heymsfield et al. (2004), which are g_0 = 0.005 13 and g_1 = 2.10.

The mass–diameter relation with the tuned coefficients is used to calculate moments of the mass equivalent sphere diameter D_e from the FSSP plus the 2D-C–HVPS size distributions (only samples with nonzero 2D-C–HVPS IWC are used). The IWC and D_{me} are derived by fitting gamma distributions: $N(D_e) \propto D_e^{\alpha} \exp[-(\alpha + 3.67)D_e/D_{me}]$, with $\alpha = 1$ to the third and fourth moments of D_e (see, e.g., Evans et al. 1998). Processing all 14 Citation flights results in temperature, IWC, and D_{me} for 13 891 samples with IWC above 0.001 g m^{-3}. The microphysical probability distribution in the Bayesian retrieval algorithm assumes a Gaussian distribution of temperature. Because the Citation sampling of temperature is experiment dependent and has nothing to do with microphysics, the microphysical samples are randomly selected to make the tempera-
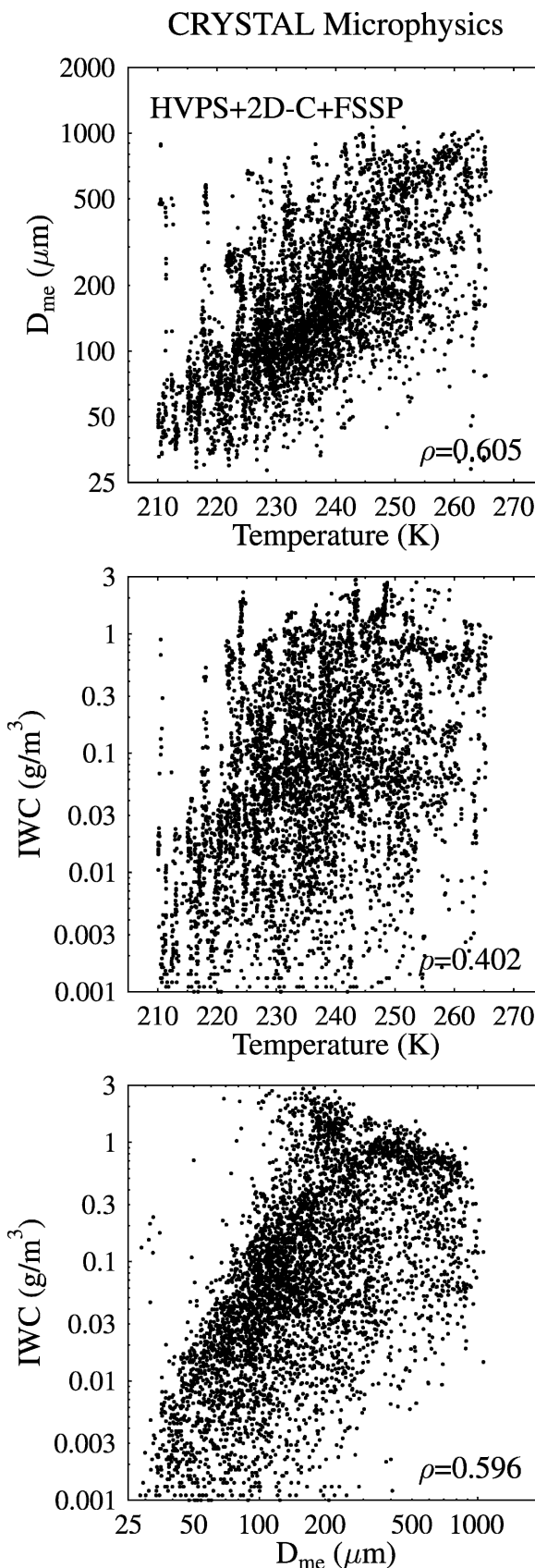
→

FIG. A2. Scatterplots of (top) D_{me} vs T, (middle) IWC vs T, and (bottom) IWC vs D_{me} derived from Citation microphysical probes. The linear correlation of the pair of variables is given in the lower right of each plot.

CRYSTAL Microphysics

TABLE A1. Microphysical input statistics

	Temperature (K)	ln(IWC) (g m^{-2})	ln(D_{me}) (μm)
Mean	236.5	−2.65	5.09
Std dev	12.2	1.82	0.766
Correlation	$\rho_{T-IWC} = 0.402$	$\rho_{T-D_{me}} = 0.605$	$\rho_{IWC-D_{me}} = 0.586$

ture distribution more Gaussian. This process outputs 5000 samples approximately matching a target distribution with a mean of 235 K and standard deviation of 15 K. Figure A2 shows the relationships between temperature, IWC, and D_{me} for these 5000 samples. Table A1 lists the statistics of temperature, ln(IWC), and ln(D_{me}), which are input to the Bayesian retrieval algorithm.

APPENDIX B

Particle Shape Modeling

The ice particle shapes that are observed during CRYSTAL FACE were most often complex irregular particles. Figure B1 shows a typical cloud particle imager (CPI) picture of the particles in a dense part of an anvil. The complex particles often appear to be aggregates of hexagonal plates. In addition, there are small, quasi-spherical particles that appear to be frozen droplets. The CoSSIR and CRS retrieval algorithms require us to model the millimeter-wave and submillimeter-wave scattering properties of distributions of these complex particles. The highest CoSSIR frequency is sensitive to features down to about 50 μm, and so it is the larger-scale particle structure about which we need to be concerned.

The CPI images inspired us to model the complex "junk ice" particles as random aggregates of hexagonal plates and columns. The algorithm for generating these particles starts with a specified number of randomly oriented hexagonal plate and column monomers of a fixed size. An aggregate particle is represented by the position and orientations of the monomers of which it is made. The particles are projected onto Z buffer images for 46 orientations, covering all viewing directions at a spacing of about 30°. A Z buffer gives the depth (positive or negative) of the particle at each pixel when viewed from a particular direction. Two particles are chosen at random to aggregate, and one of the 46 orientations is also chosen at random for each particle. The two-particle Z buffers for these orientations and a random sideways offset between the two particles are used to determine when the particles touch (a certain amount of overlap may be specified). The two particles are then combined by rotating the first particle to the second particle's coordinates to make a new aggregate particle. The Z buffer images are made for the new aggregated particle. This process of aggregating (potentially already aggregated) particles proceeds until there

is only one particle left, which contains all of the original monomers.

Three sets of random hexagonal aggregate particles are created. The first set of 20 sizes of the hexagonal plate aggregates has monomers with a maximum diameter of 230 μm and a thickness of 25 μm. The second set of 20 sizes of plate aggregates has thicker plates with a maximum diameter of 210 μm and a thickness of 30 μm. The last set has plates (diameter of 230 μm and thickness of 25 μm) for 75% of the monomers and hexagonal columns (diameter of 115 μm and length of 300 μm) for 25% of the monomers (18 particle sizes). Figure B2 shows one example particle image from each of the three sets. The maximum number of monomers that is modeled is determined by the computational limits of the light-scattering code. Table B1 lists the orientation average maximum diameter, equivalent volume sphere diameter, and equivalent area sphere diameter for the smallest (a single monomer) and largest aggregate of each type. Despite the computational limit, the average maximum diameter ranges up to 1.5–1.8 mm, depending on the type of aggregate. The plate/column aggregates are supplemented with seven solid ice spheres with diameters from 20 to 80 μm to simulate the quasi-spherical particles that are seen in the CPI images.

CPI images from the WB-57, which flew at higher altitudes than the Citation, show chains of quasi-spherical particles, perhaps aggregated by the electric fields in the anvil tops. The more convective parts of these cloud systems are likely to have graupel particles. Both of these particle types can be modeled by random aggregates of small ice spheres. The random sphere aggregation algorithm is similar to the hexagonal plate and column aggregation method, but simpler. The spheres are sent into the particle one at a time, so that there is no aggregation of aggregates. For this work, each sphere monomer is sent into a random orientation of the particle (however, a fixed orientation gives a nice conical-shaped graupel particle). Two sets of random sphere aggregates are made with two sizes of monomer spheres (30 and 40 μm). Over the 23 sizes of sphere aggregates the number of monomers ranges up to 3600, the average maximum diameter goes up to 1.00 or 1.32 mm (for 30- or 40-μm spheres), and the equivalent volume diameter ranges up to 0.460 or 0.613 mm. Figure B3 shows two of the sphere aggregate particles.

The single-scattering information for the randomly oriented particles described above is computed with the discrete dipole approximation (DDA) at the frequen-
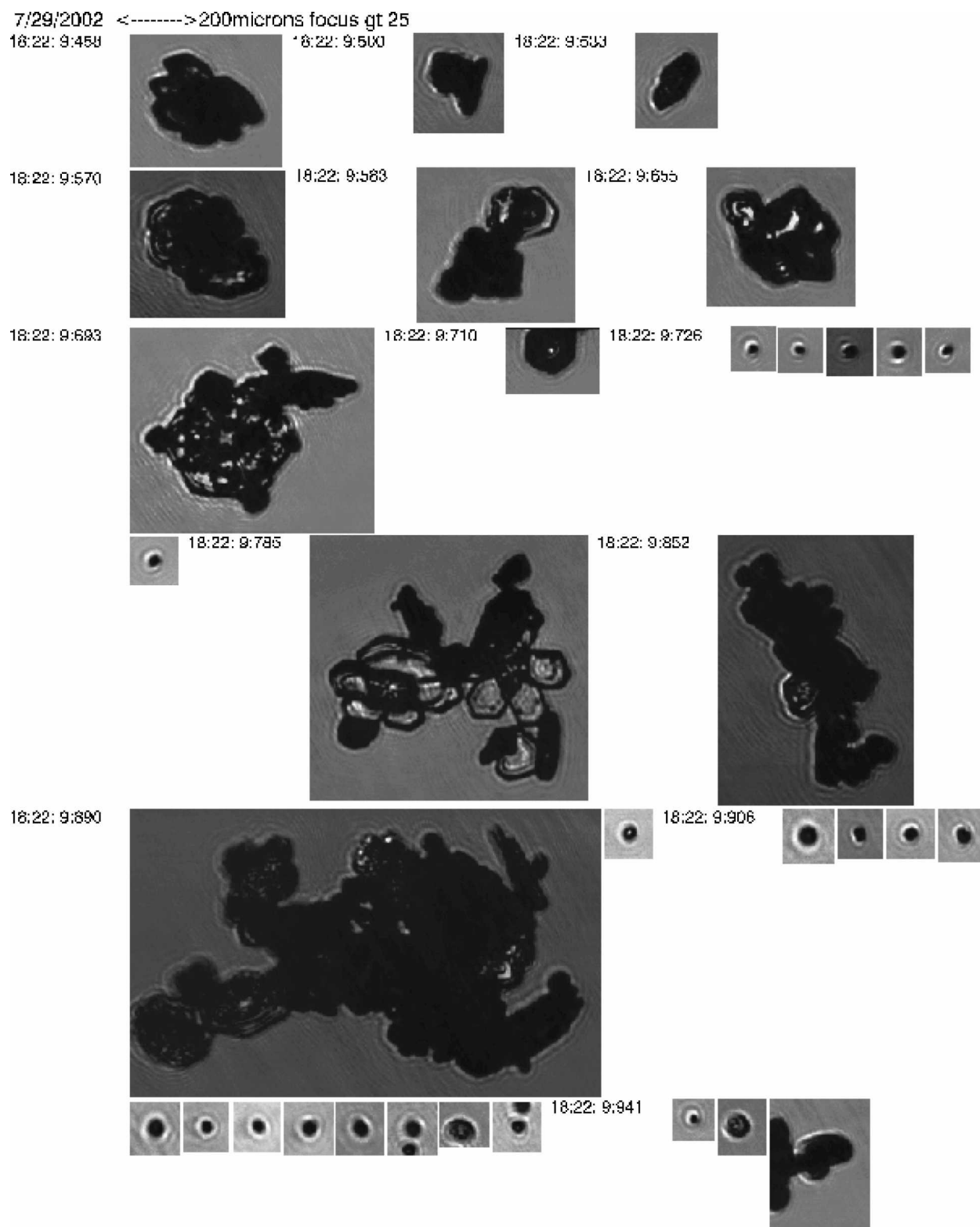
FIG. B1. A Citation cloud particle imager display showing ice particle shapes from a thick anvil region at 1822:10 UTC 29 Jul. The numbers next to each picture give the exact time. A scale is shown at the top.

FIG. B2. Some Z-buffer images showing one particle from each of the three sets of random hexagonal aggregates. (top) An aggregate of 6 of the thinner plates, (middle) an aggregate of 20 plates and columns, and (bottom) an aggregate of 40 thicker plates. The lighter shades indicate the closer parts of the particle, and the darker shades indicate the farther parts.

cies of CoSSIR and CRS [see Evans and Stephens (1995a) for a description of the DDA code]. A particle is divided into a number of dipoles; for the sphere aggregates each sphere monomer is a dipole, while for the hexagonal aggregates the dipole size is equal to the plate thickness. The dipoles are arrayed on a lattice

TABLE B1. Diameter statistics for the random hexagonal aggregate particles; N_{mono} is the number of monomers from which the aggregate is made, $\langle D_{max}\rangle$ is the average maximum particle extent over 46 orientations, D_{eqvol} is the volume equivalent sphere diameter, and D_{eqarea} is the area equivalent sphere diameter. The shape plate 1 refers to the thinner plate aggregates, plate 2 refers to the thicker plate aggregates, and plate column refers to the aggregates of 75% plates and 25% columns.

Shape	N_{mono}	$\langle D_{max}\rangle$ (mm)	D_{eqvol} (mm)	D_{eqarea} (mm)
Plate 1	1	0.183	0.118	0.165
Plate 1	40	1.566	0.451	1.017
Plate 2	1	0.162	0.118	0.155
Plate 2	76	1.858	0.553	1.222
Plate column	40	1.493	0.462	0.913

oriented along each hexagonal plate or column monomer, and grid cells with more than one-half of their volume inside the particle have a dipole assigned (partial volume dipoles with a reduced index of refraction are not used). This method of allocating dipoles at arbitrary positions requires using the DDA matrix inversion method. The inversion method is actually far faster than the fast Fourier transform–conjugate–gradient solution method, because the latter requires a uniform lattice of dipole sites (hence, many more partially filled dipoles) and the solution method must be repeated for each incident direction. The maximum number of dipoles, however, is limited to 3600 for a computer with 1 GB of memory (because of the $3N \times 3N$ complex dipole interaction matrix for N dipoles). The orientation
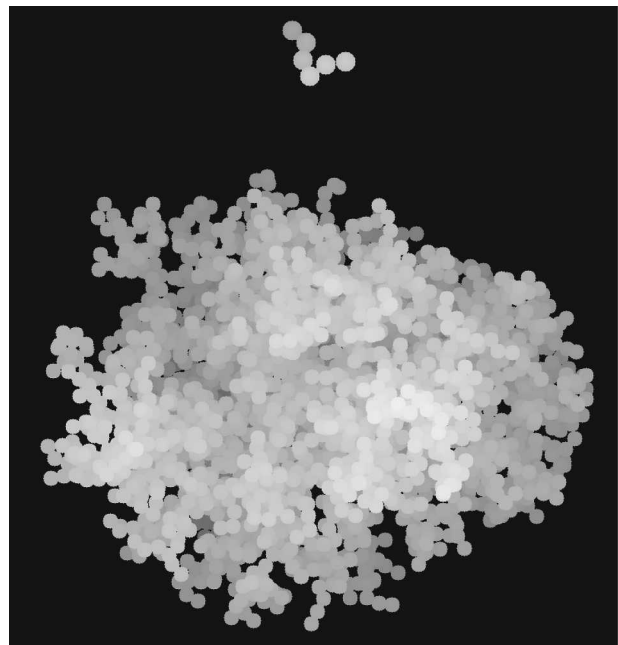

FIG. B3. Some Z-buffer images showing two random sphere aggregate particles. (top) An aggregate of 6 spheres (40-μm diameter), and (bottom) an aggregate of 3600 spheres (30-μm diameter).

average is performed with incident directions at 16 zenith angles times 32 azimuth angles. Although these random aggregate particles would not be expected to be completely randomly oriented, the fast Eddington radiative transfer model requires random orientation, so that the single scattering properties are defined by the extinction, single scattering albedo, and asymmetry parameter.

Figure B4 shows the three scattering properties for the lowest and highest CoSSIR frequencies as a function of the equivalent volume sphere diameter D_e. There is a significant, but modest, difference in extinction and single scattering albedo between sphere aggregates and hexagonal aggregates for D_e above about 150 μm. There is a large difference, however, in the asymmetry parameter between the particle shapes, which affects the CoSSIR radiances substantially.

Even though the average maximum diameter of the largest sphere aggregate (with 3600 spheres) is above 1 mm, particles with D_e larger than 600 μm are needed for the deeper, more convective parts of the clouds. Given the computational limits of the DDA method, we chose to calculate the scattering properties of larger sphere aggregates with a tuned effective medium approximation. Effective medium approximations use "mixing rules" to calculate an effective index of refraction for the mixture of ice and air in a heterogenous particle. These theories assume a uniform mixture with ice (or air) inclusions that are very small compared to the wavelength (e.g., Chylek et al. 2000). Because these assumptions are violated for ice particles at submillimeter wavelengths, it is best to use mixing rules in an empirical fashion. In addition to the choice of a particular mixing rule, one can also choose the diameter of the sphere to represent the nonspherical particle (and, hence, the volume fraction of ice to use in the mixing rule). The approach taken here is to try several mixing rules and several definitions of effective diameter and to choose the best combination for matching Mie theory to the DDA scattering results. Then, the Mie theory mixing rule method is used to extrapolate the scattering results to larger D_e for the sphere aggregate particles. The following mixing rules were tried: the Lorentz–Lorenz, Bruggeman, and inverse Maxwell–Garnett (air inclusions in ice). The Lorentz–Lorenz mixing rule is defined by

$$\frac{\varepsilon_{\text{eff}} - 1}{\varepsilon_{\text{eff}} + 2} = v \frac{\varepsilon_i - 1}{\varepsilon_i + 2}, \qquad (B1)$$

where $\varepsilon_{\text{eff}} = m_{\text{eff}}^2$ is the effective dielectric constant, m_{eff} is the effective index of refraction, ε_i is the dielectric constant of ice, and v is the ice volume fraction. The effective diameters that were tried include the equivalent volume sphere diameter (i.e., an ice volume fraction of unity), the average maximum diameter, the root-mean-square weighted diameter, the root-mean-cubed weighted diameter, and the root-mean-sixth-
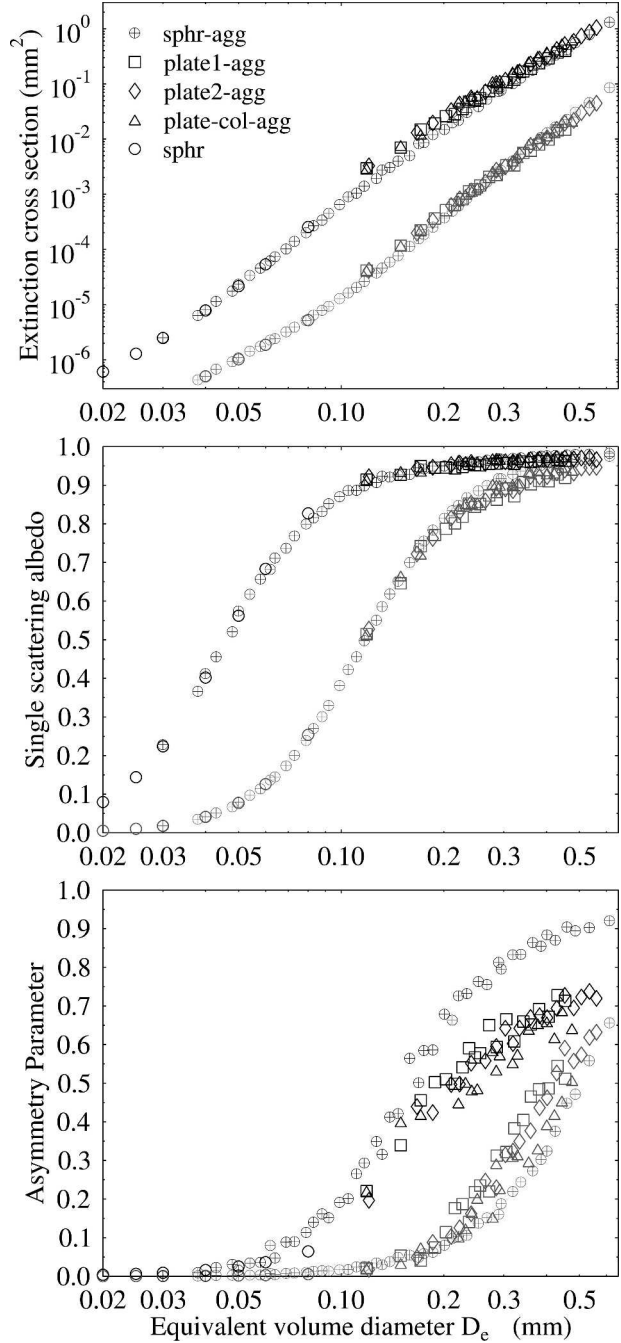

FIG. B4. The (top) extinction, (middle) single-scattering albedo, and (bottom) asymmetry parameter for the four random aggregate particle shapes at 183 (light gray) and 640 (black) GHz. The small spheres that supplement the hexagonal aggregates are also shown. The aggregates with 30- and 40-μm spheres are combined into one particle type.

moment weighted diameter. The latter three diameters are defined by

$$D_{\text{rm},n} = 2 \left(\frac{1}{N} \sum_{i=1}^{N} r_i^n \right)^{1/n}, \qquad (B2)$$

where r_i is the distance of the sphere monomer from the center of mass, N is the number of sphere monomers, and n is 2, 3, or 6.

Figure B5 shows the most relevant results comparing Mie theory with a mixing rule to the DDA scattering results for sphere aggregates. Using Mie theory for solid ice spheres (diameter equal to D_e) gives an extinction that is much too high and an asymmetry parameter that is much too low. Using the average maximum diameter (a reasonable way to define the actual diameter of a sphere aggregate) and the Lorentz–Lorenz mixing rule results in the extinction being too low and the asymmetry parameter being too high. The best effective diameter definition is the sixth-moment weighted diameter, which gives accurate results, especially above $D_e = 0.3$ mm, where the aggregate is made up of a large number of spheres. The Bruggeman mixing rule results are quite similar to those of Lorentz–Lorenz, while the inverse Maxwell–Garnett mixing rule does not work well and is also not very physical. The sphere aggregate scattering properties are then extended to larger sizes by creating each random aggregate particle (up to 60 000 sphere monomers), calculating the sixth-moment diameter D_{rm6} and the corresponding volume fraction, determining the Lorentz–Lorenz effective index of refraction, and computing the Mie scattering properties.

The Bayesian retrieval database should include different shapes at all particle sizes (D_e), so that there is realistic variability in this radiatively important parameter. However, with the particle shapes described above, there are only sphere aggregates for $D_e > 0.55$ mm. To increase the variability in scattering properties for the larger particle sizes, a fifth particle type is modeled—low density spheres, perhaps representing snow aggregates. The volume fraction of the sphere aggregates at the largest sizes is 0.22–0.24 (using the D_{rm6} diameter), so we choose a volume fraction of 0.1. The Lorentz–Lorenz mixing rule and Mie theory are used to compute the scattering properties of these low-density spheres for D_e from 0.080 to 1.60 mm.

For each particle type the computed scattering properties are summed over gamma distributions of the particle sizes. The gamma distributions are defined by $N(D_e) \propto D_e^\alpha \exp[-(\alpha + 3.67)D_e/D_m]$ where D_e is the equivalent sphere diameter. To deal with the truncation of the size distribution from the finite range of particle sizes, D_{me} and α for a discrete distribution are adjusted so that the fourth and sixth moments (in addition to the IWC) match those of a theoretical continuous gamma distribution with the desired D_{me} and α. The D_{me} and α calculated from the moments must match the desired values within specified tolerances (2% for D_{me} and 0.5 in α are used here). This limits the range of allowed D_{me} in a scattering table made for a particular particle type and α. As shown in Table B2 the narrowest distribution $\alpha = 7$ has the largest range of D_{me}. The available D_{me} in the scattering tables affects the distribution
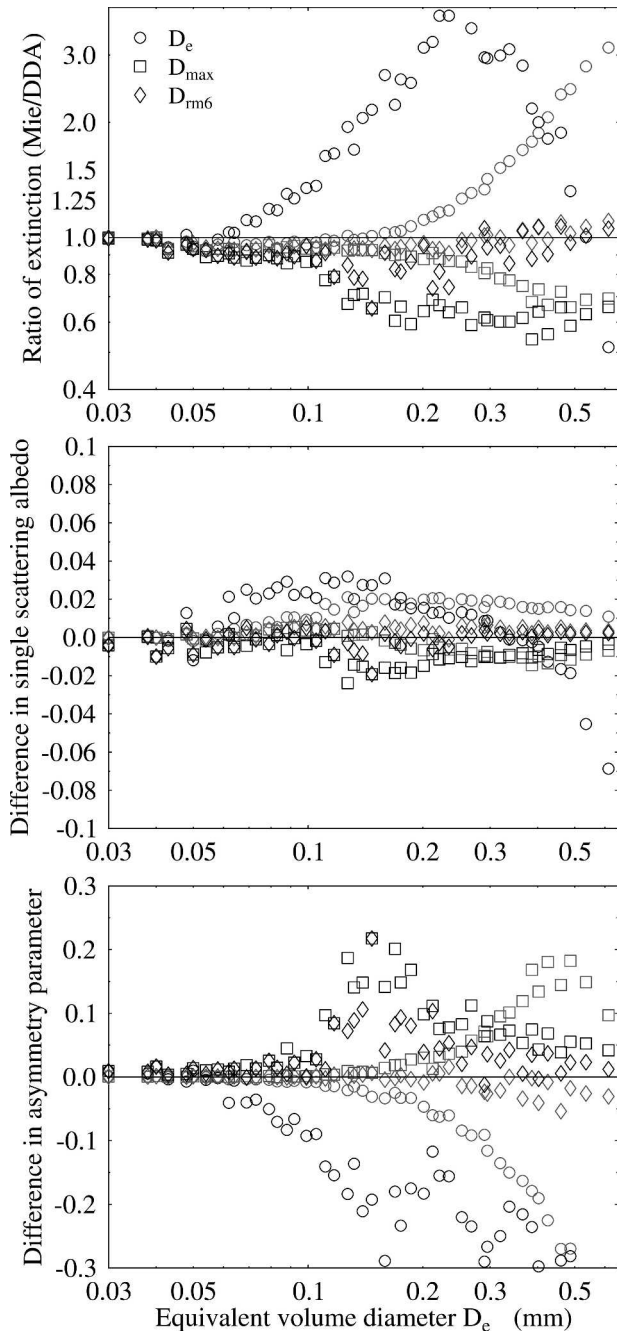

FIG. B5. The errors in (top) extinction, (middle) single-scattering albedo, and (bottom) asymmetry parameter from using Mie theory to approximate the scattering properties of random sphere aggregates (computed with DDA). The points labeled D_e (circles) are for Mie theory with no mixing rule on spheres having the equivalent volume sphere diameter. The points labeled D_{max} (squares) are for Mie theory with the Lorentz–Lorenz mixing rule on spheres having the average maximum aggregate diameter. The points labeled D_{rm6} (diamonds) are for Mie theory with the Lorentz–Lorenz mixing rule on spheres having the sixth-power weighted diameter. Light gray symbols are for 183 GHz, and black symbols are for 640 GHz.

TABLE B2. Range of D_{me} (μm) in scattering tables, and minimum and maximum D_{me} in the 15 scattering tables used in the retrievals; "sphr(vf = 0.1)" refers to the low-density spheres with volume fraction of 10% ice. The hexagonal plate–column aggregate distributions also include small solid ice spheres (20–80-μm diameter). The scattering tables have D_{me} steps of a factor of $2^{1/6}$ (about 0.5 dB). Here, "agg" indicates aggregate.

Shape	$\alpha = 0$		$\alpha = 2$		$\alpha = 7$	
	Min	Max	Min	Max	Min	Max
Sphr(vf = 0.1)	126	800	112	898	100	1270
Sphr agg	50	713	45	898	40	1131
Plate 1–agg	32	225	28	252	25	318
Plate 2–agg	32	252	28	318	25	400
Plate column–agg	32	225	28	283	25	318

of clouds in the retrieval database because randomly selected clouds that have a D_{me} at cloud top or base outside of the allowed range for the randomly chosen scattering table are rejected.

REFERENCES

Chylek, P., G. Videen, D. J. W. Geldart, J. S. Dobbie, and H. C. W. Tso, 2000: Effective medium approximations for heterogeneous particles. *Light Scattering by Nonspherical Particles: Theory, Measurement, and Applications,* M. I. Mishchenko, J. W. Hovenier, and L. D. Travis, Eds., Academic Press, 274–308.

Deeter, M. N., and K. F. Evans, 2000: A novel ice-cloud retrieval algorithm based on the millimeter-wave imaging radiometer (MIR) 150- and 220-GHz channels. *J. Appl. Meteor.,* **39,** 623–633.

Durden, S. L., E. Im, F. K. Li, W. Picketts, A. Tanner, and W. Wilson, 1994: ARMAR: An airborne rain-mapping radar. *J. Atmos. Oceanic Technol.,* **11,** 727–737.

Evans, K. F., and G. L. Stephens, 1995a: Microwave radiative transfer through clouds composed of realistically shaped ice crystals. Part I: Single scattering properties. *J. Atmos. Sci.,* **52,** 2041–2057.

——, and ——, 1995b: Microwave radiative transfer through clouds composed of realistically shaped ice crystals. Part II: Remote sensing of ice clouds. *J. Atmos. Sci.,* **52,** 2058–2072.

——, S. J. Walter, A. J. Heymsfield, and M. N. Deeter, 1998: Modeling of submillimeter passive remote sensing of cirrus clouds. *J. Appl. Meteor.,* **37,** 184–205.

——, ——, ——, and G. M. McFarquhar, 2002: The submillimeter-wave cloud ice radiometer: Simulations of retrieval algorithm performance. *J. Geophys. Res.,* **107,** 4028, doi:10.1029/2001JD000709.

Gasiewski, A. J., 1992: Numerical sensitivity analysis of passive EHF and SMMW channels to tropospheric water vapor, clouds, and precipitation. *IEEE Trans. Geosci. Remote Sens.,* **30,** 859–870.

Heymsfield, A. J., A. Bansemer, C. Schmitt, C. Twohy, and M. R. Poellot, 2004: Effective ice particle densities derived from aircraft data. *J. Atmos. Sci.,* **61,** 982–1003.

Li, L., G. M. Heymsfield, P. E. Racette, T. Lin, and E. Zenker, 2004: A 94-GHz cloud radar system on a NASA high-altitude ER-2 aircraft. *J. Atmos. Oceanic Technol.,* **21,** 1378–1388.

Liu, G., and J. A. Curry, 2000: Determination of ice water path and mass median particle size using multichannel microwave measurements. *J. Appl. Meteor.,* **39,** 1318–1329.

Racette, P., R. F. Adler, J. R. Wang, A. J. Gasiewski, D. M. Jackson, and D. S. Zacharias, 1996: An airborne millimeter-wave imaging radiometer for cloud, precipitation, and atmospheric water vapor studies. *J. Atmos. Oceanic Technol.,* **136,** 610–619.

Rossow, W. B., and R. A. Schiffer, 1999: Advances in understanding clouds from ISSCP. *Bull. Amer. Meteor. Soc.,* **80,** 2261–2287.

Sekelsky, S. M., and R. E. McIntosh, 1996: Cloud observations with polarimetric 33 GHz and 95 GHz radar. *Meteor. Atmos. Phys.,* **59,** 123–140.

Stephens, G. L., and Coauthors, 2002: The CloudSat mission and the Atrain: A new dimension of space-based observations of clouds and precipitation. *Bull. Amer. Meteor. Soc.,* **83,** 1771–1790.

Stubenrauch, C., R. Holz, A. Chedin, D. L. Mitchell, and A. J. Baran, 1999: Retrieval of cirrus ice crystal sizes from 8.3 and 11.1 micron emissivities determined by the improved initialization inversion of TIROS-N Operational Vertical Sounder observations. *J. Geophys. Res.,* **104,** 793–808.

Twohy, C., A. J. Schanot, and W. A. Cooper, 1997: Measurement of condensed water content in liquid and ice clouds using an airborne counterflow virtual impactor. *J. Atmos. Oceanic Technol.,* **14,** 197–202.

Valenzuela, G. R., 1978: Theories for the interaction of electromagnetic and oceanic waves: A review. *Bound.-Layer Meteor.,* **13,** 61–85.

Vanek, M. D., and Coauthors, 2001: Far infrared sensor for cirrus (FIRSC): An aircraft-based FTS to measure the earth radiance spectrum. *Appl. Opt.,* **40,** 2169–2176.

Wang, J. R., P. Racette, J. D. Spinhirne, K. F. Evans, and W. D. Hart, 1998: Observations of cirrus clouds with airborne MIR, CLS, and MAS. *Geophys. Res. Lett.,* **25,** 1145–1148.

——, G. Liu, J. D. Spinhirne, P. Racette, and W. D. Hart, 2001: Observations and retrievals of cirrus cloud parameters using multichannel millimeter-wave radiometric measurements. *J. Geophys. Res.,* **106** (D14), 15 251–15 263.

Weng, F., and N. C. Grody, 2000: Retrieval of ice cloud parameters using a microwave imaging radiometer. *J. Atmos. Sci.,* **57,** 1069–1081.

Wielicki, B. A., R. D. Cess, M. D. King, D. A. Randall, and E. F. Harrison, 1995: Mission to Planet Earth: Role of clouds and radiation in climate. *Bull. Amer. Meteor. Soc.,* **76,** 2125–2153.